

THE MAGNETIC FIELD STRUCTURE OF THE LMC 2 SUPERSHELL: NGC 2100

JOHN P. WISNIEWSKI^{1,2,3}, KAREN S. BJORKMAN^{3,4}, ANTONIO M. MAGALHÃES^{3,5}, ANTONIO PEREYRA⁵*Accepted for publication in ApJ - Draft version February 1, 2008*

ABSTRACT

We present U,B,V,R,I imaging polarimetry of NGC 2100 and its surrounding environment, which comprise a part of the LMC 2 supershell. The morphology of the observed position angle distribution provides a tracer of the projected magnetic field in this environment. Our polarization maps detail regions exhibiting similarly aligned polarization position angles, as well as more complex position angle patterns. We observe regions of coherent fields on spatial scales of 42 x 24 pc to 104 x 83 pc, and infer projected field strengths of \sim 14-30 μ G. We propose that the superposition of global outflows from the LMC 2 environment, as well as outflows created within NGC 2100, produce the unique field geometry in the region.

Subject headings: ISM: bubbles — ISM: magnetic fields — Magellanic Clouds — open clusters and associations: individual (NGC 2100) — techniques: polarimetric — stars: individual (HIP 21556)

1. INTRODUCTION

Magnetic fields are known to align dust grains, hence influence astrophysical processes, in a wide variety of environments (see e.g. Goodman 1996; Lazarian 2003). The alignment of grains in the diffuse interstellar medium of the Milky Way (Mathewson & Ford 1970a) and the Magellanic Clouds (Mathewson & Ford 1970b) has long been known from linear polarization studies, which measure the dichroic absorption of starlight. Similarly, polarimetric observations indicate grains may also be aligned in environments such as dark clouds (Lazarian et al. 1997; Hildebrand et al. 1999), and the circumstellar environments of young (Aitken et al. 1993; Tamura et al. 1999) and old (Aitken et al. 1995) stars. As reviewed within Lazarian (2003), a number of alignment mechanisms have been proposed over the past sixty years, and it is likely that the local conditions of each astrophysical environment will dictate the relative importance of each of these proposed alignment mechanisms. Characterizing the typical polarimetric behavior in each of these environments offers one avenue to constrain the relative importance of these mechanisms in each environment.

Massive stars in OB associations provide a rich source of outflows from stellar winds and supernovae explosions; the interaction of such outflows with the surrounding interstellar medium (ISM) is known to create large supershells. Observations suggest that some of these shells may be magnetized, with typical fields strengths of at least several to tens of μ G (Vallee 1993, 1994; Pereyra & Magalhães 2007), and it is expected that these fields can influence the dynamical evolution of shells, including constraining their expansion (Mineshige et al. 1993; Tomisaka 1998). With a diameter of \sim 900 pc, LMC 2 was initially identified as a supershell based upon its morphology (Meaburn 1980). The kinematics of the LMC 2 supershell has been a subject of some debate: Caulet et al. (1982) suggested that

LMC 2 was expanding as a cohesive structure; however, followup studies by Meaburn et al. (1987), Points et al. (1999) and Ambrocio-Cruz et al. (2004) argue against a global expansion, asserting the structure is a conglomeration of localized expanding structures. Observed extended X-ray emission in the region led Wang & Helfand (1991) to suggest that LMC 2 was formed as a result of a superbubble breaking out from the plane of the Large Magellanic Cloud (LMC).

The richest of the 29 stellar associations in the direction of LMC 2 identified by Hodge & Wright (1967) projected to lie interior to LMC 2 is NGC 2100. Given its age, \sim 15 Myr (Cassatella et al. 1996), Points et al. (1999) has postulated that all of NGC 2100's O stars have exploded as supernovae, implying that it has played an important role in shaping the observed structure of LMC 2. Points et al. (1999) and Ambrocio-Cruz et al. (2004) observed complex H α velocity components which vary across the extent of NGC 2100, suggesting the presence of a turbulent interstellar environment. The interstellar polarization near NGC 2100 is also known to differ from general behavior of the LMC (0.32 - 0.57% at position angles of 28-45°, Wisniewski 2005; Wisniewski et al. 2007); Mathewson & Ford (1970b) observed a strong focusing of magnetic lines around 30 Doradus (30 Dor), which is located \sim 16' west of the LMC 2 supershell.

In this paper, we present detailed polarization maps of NGC 2100 and its surrounding environment, which reveal evidence of a complex magnetic field morphology. These data provide diagnostics of the grain alignment mechanisms which likely dominate in such dynamic astrophysical environments. In Section 2, we describe our polarimetric observations. Polarization maps and estimates of projected magnetic field strengths are presented in Section 3. In Section 4, we present a discussion of these results and the clues they may offer towards understanding the

¹ NASA GSFC Code 667, Greenbelt, MD 20771 USA, jwisnie@milkyway.gsfc.nasa.gov² NPP Fellow³ Visiting Astronomer, Cerro Tololo Inter-American Observatory⁴ Ritter Observatory, Department of Physics and Astronomy MS 113, University of Toledo, Toledo, OH 43606, karen.bjorkman@utoledo.edu⁵ IAG, Universidade de São Paulo, Caixa Postal 3386, São Paulo, SP 01060-970, Brazil, mario@astro.iag.usp.br, antonio@astro.iag.usp.br

formation and evolution of the LMC 2 supershell.

2. OBSERVATIONS

Imaging polarimetry of NGC 2100 and its surrounding field were obtained at the CTIO 1.5 m telescope, as summarized in Table 1. We used the F/7.5 secondary configuration, yielding a 15'0 field of view and a 0''.44 pixel⁻¹ scale. Data were recorded with the telescope's standard Cassegrain focus CCD (CFCCD), a 2048 x 2048 CCD which was read out in dual amplifier mode. The standard telescope configuration was modified by the addition of a rotatable half-wave plate, followed by a dual calcite block (Savart plate) placed in the first filter wheel. This dual calcite analyzer, whose optical axes were crossed to minimize astigmatism and color effects, simultaneously produced two orthogonally polarized images of all objects, allowing for the near complete cancellation of all background sky polarization, as well as atmospheric transparency effects (Magalhães et al. 1996). A small imperfection in the calcite block was masked out, shrinking the effective field of view of the instrument by 2'0-3'0 arcminutes in the southeast corner of the CCD and by \sim 1.5' in the northeast and northwest corners of the chip. Standard Johnson U, B, V, R, and I filters were housed in the second filter wheel. Images were taken at 8 wave-plate positions, each separated by 22.5°, allowing us to derive full linear polarization measurements for NGC 2100. Additional information regarding this instrument can be found in Magalhães et al. (1996), Melgarejo et al. (2001), and Pereyra & Magalhães (2002).

Basic image processing was done in IRAF⁶ using standard techniques. After deriving aperture photometry for our images, the least squares solution of the 8 wave-plate positions, calculated with the PCCDPACK polarimetric reduction package (Pereyra 2000), yielded linear polarization measurements. The residuals at each wave-plate position, ψ_i , with respect to the expected $\cos 4\psi_i$ curve constitute the uncertainties in our data; these are consistent with the theoretically expected photon noise errors (Magalhães, Benedetti, & Roland 1984).

Instrumental polarization effects were determined from observations of polarized and unpolarized standard stars, obtained nightly during our ten day observing run in 2001. These data are self-consistent and agree with observations obtained in a subsequent eleven day observing run in 2002 (Wisniewski et al. 2003) using the same instrument, illustrating its excellent stability. The instrumental polarization was measured to be within 0.03% (I filter) to 0.07% (B filter), thus no correction was applied to our data. Note that due to a lack of known faint unpolarized standard stars, we used the M star HIP 21556 as an unpolarized standard star for the B, V, R, and I filters. Given its nearby location ($d=11$ pc) and spectral type, one would not expect such an object to exhibit significant polarization (Tinbergen 1982). Indeed, observations of this target during our 2001 and 2003 observing runs showed it to be unpolarized.

3. RESULTS

The polarization data we discuss represent the superposition of two components of distinctly different origin, namely interstellar and intrinsic polarization. Intrinsic polarization can arise from a variety of scattering mechanisms within the circumstellar environment of a host star, while interstellar polarization results from dichroic absorption of starlight by aligned interstellar dust grains located along the line of sight. Most of our targets should be normal main-sequence stars which are not characterized by the presence of an extended (or asymmetrical) circumstellar envelope, hence they will exhibit no intrinsic polarization at the precision level of our measurements. The statistical analysis of the total polarization observed for each of our targets should thus provide an accurate diagnostic of the interstellar polarization along the line of sight (McLean & Clarke 1979; Pereyra & Magalhães 2002; Wisniewski et al. 2003, 2007). Furthermore, given the LMC's large distance of 50 kpc (Feast 1991), any spatial variability we detect in this interstellar polarization component must be the result of a change in the magnetic field or interstellar dust grain properties within the LMC, rather than a projection of Galactic interstellar medium properties.

3.1. Polarization Maps

In Figures 1-5 we present the polarization in the U, B, V, R, and I filters for NGC 2100 and its surrounding field. Polarization vectors are overplotted on Digitized Sky Survey2 (DSS2) red (V, R, and I filters) and blue (U and B filters) images which span 0.5 square degrees, allowing one to place the polarization of NGC 2100 in the context of the LMC 2 supershell. A more detailed image of LMC 2's nebulosity, including identification of the major OB associations in the area, can be seen in Figure 1c of Points et al. (1999). To exclude likely spurious detections, we have only plotted objects with the following properties: $0.1\% < \text{polarization} < 3.0\%$ and $p/\sigma_p > 3.0$.

Numerous trends in the morphology of the polarization vectors in each of the filters can immediately be seen. The magnitude of a typical polarization vector is $\sim 1.5\%$, which is significantly higher than the average polarization observed throughout the LMC (Wisniewski 2005; Wisniewski et al. 2007). While polarization position angles (PA) tend to be coherent on small spatial scales, large-scale variability across the field of view of the data set is immediately apparent. The patterns traced by this large-scale variability are consistent across every filter, indicating the phenomena represent real features.

To further explore these large-scale position angle trends, we divided our field of view into 5 smaller spatial scales which each seemed to possess one unique, average position angle. We assign the arbitrary labels A-E to these fields, and show these fields in the R filter in Figures 6-10. Note that we have only plotted all objects with $0.1\% < \text{polarization} < 3.0\%$ and $p/\sigma_p > 3.0$ in these figures. The mean position angle, FWHM of gaussian fits to the samples, standard deviation (in radians) of objects within the gaussian fit for each area, and spatial extent of each area, assuming a distance of 50 kpc, are tabulated in Table 2. The polarization position angle histograms used to derive

⁶ IRAF is distributed by the National Optical Astronomy Observatories, which are operated by the Association of Universities for Research in Astronomy, Inc., under contract with the National Science Foundation.

these parameters are also given in Figures 6-10.

The position angle rotation to the north, west, and south of NGC 2100, apparent by casual inspection of Figures 1-5, is indeed real as we measure the mean PA to vary from 76° to 122° to 94° in Figures 7-9 respectively. Figure 10 depicts spatial area E, immediately west of NGC 2100, showing PA alignment at 167° . The dramatic curvature in the field pattern traced out in areas B-E in the area west of NGC 2100 qualitatively matches a similar “bubble-like” pattern seen in the $\text{H}\alpha$ image of the LMC 2 region of Points et al. (1999), e.g. their Figure 1a.

Systematic alignment in the eastern portion of our field of view is less dramatic, as seen in Figure 6 which depicts area A. We find position angles in area A tend to be $< 90^\circ$, and find suggestive evidence that the PA distribution in this spatial region may be fit by two gaussians at 29° (FWHM = 25°) and 64° (FWHM = 22°) respectively. The constituents of these two possible gaussian distributions occupy no unique spatial regions: it is possible that the observed distributions originate at slightly different distances within the LMC 2 neighborhood, projecting themselves onto common spatial regions. Alternatively, it is possible that large-scale LMC-2 flows to the west of NGC 2100 are interacting with velocity fields from within NGC 2100 to produce the observed apparent superposition effects.

The projected spatial extent of regions with definitive, coherent position angle alignment varies from 42×24 pc, associated with region E, to 104×83 pc, associated with region B. We note the suggestive presence of smaller alignment trends within and outside of some of these designated areas. Due to small number statistics, it is unclear whether such features are real, hence illustrating common alignment on finer scales, or whether they are the result of small intrinsic polarization components adding small scatter to the data set. Deeper polarimetric mapping of the region would clarify the presence of small-scale alignment by providing a larger statistical database. If our polarization maps are indeed tracing some of the larger structures in the $\text{H}\alpha$ maps of Points et al. (1999), then we would expect deeper polarization maps to trace many of the finer nebulosity seen in such images.

3.2. Estimating B Fields

A formalism for estimating magnetic field strengths from polarimetric observations was developed by Chandrasekhar & Fermi (1953)(C-F technique), and has been since modified to account for various inadequacies (see e.g. Goodman (1996); Zweibel (1996); Heitsch et al. (2001); Crutcher (2004)). As summarized by Heitsch et al. (2001); Henning et al. (2001) and Pereyra & Magalhães (2007), while the C-F method is a commonly used technique to estimate magnetic field strengths, its use is dubious in cases of, amongst other factors, large polarization position angle dispersions and large turbulent velocity dispersions. We have used the description provided by equation 7 of Heitsch et al. (2001),

$$B = \frac{1}{2} \sqrt{4\pi\rho \left(\frac{\sigma(v_{los})^2}{\sigma(\tan\delta)^2} \right)} \quad (1)$$

, where ρ is the mean density, $\sigma(v_{los})$ is the dispersion in the line-of-sight velocity, and $\sigma(\tan\delta)$ is the dispersion in

polarization position angles, i.e. the difference, within the distribution, between the position angle of a given object and the average position angle. This description was used as it eliminates the small angle approximation present in the original formalism; furthermore, it includes a factor of $1/2$ to account for the field overestimation provided by the classical Chandrasekhar-Fermi method (Crutcher 2004).

We were able to measure position angle dispersions for regions B-E of our dataset using PCCDPACK and tabulate the standard deviation of these values, $\sigma(\tan\delta)$ in Table 2. Points et al. (1999) reported a HI number density of $3-4 \text{ cm}^{-3}$: we assumed a number density of 4 cm^{-3} in our calculations. We estimated the line of sight velocity for our regions from the HI velocities reported by Meaburn et al. (1987) for their region 43, corresponding to the approximate location of NGC 2100, $\sigma_{vlos} = 52 \text{ km s}^{-1}$. This dispersion is consistent with the FWHM of $\text{H}\alpha$ velocities reported by Points et al. (1999) across their E-I spectroscopic cut. The resulting magnetic field strengths for our fields range from $14-30 \mu\text{G}$, as tabulated in Table 2. We stress that these field values should only be considered crude estimates: detailed measurements of the gas velocity dispersions and densities corresponding to the specific spatial regions in which we observed polarization position angle dispersions are needed to further refine these field estimates. Nevertheless, our derived range of field strengths are consistent with the strength of random field fluctuations in the LMC reported by Gaensler et al. (2005), especially those located nearby supernova remnants and wind bubbles, which were quoted to be $\sim 8 \mu\text{G}$ by these authors.

4. DISCUSSION

We now explore some of the implications of the polarization maps presented in Section 3.1. Our polarization maps of NGC 2100 and its nearby environment indicate the presence of a sizable magnitude of interstellar polarization, $\sim 1.5\%$ which experiences systematic position angle changes. We attribute this position angle variability to changes in the orientation of the projected magnetic field. It is equally likely that the third dimension of this field also varies. The only effect such a variation would have on our data set would be additional dispersion in the distribution of polarization levels. While a wide distribution is observed, other factors such as the presence of small intrinsic polarization components in objects, small variability in the distance of objects within our field of view, and changes in the polarizing properties of the grains across the field of view, i.e. changes in grain size, shape, or composition, also likely serve to broaden the observed distribution. Additional observational tools, such as that provided by atomic alignment (Yan & Lazarian 2006), could be used to provide an independent measure of the localized three-dimensional magnetic field.

4.1. Origin of Position Angle Variations

We consider the origin of the position angle variability detailed in Section 3.1. Given the dynamic nature of the region, it seems plausible to expect the complex field patterns, which align grains to produce the observed polarization, to be driven by the various outflows present. Such a scenario is supported by the possible tracing of large $\text{H}\alpha$ features by our data, as noted in Section 3.1. The

morphological details of Figures 1-5 suggest that the field patterns are not solely guided by the stellar outflows and supernovae remnants of NGC 2100. Studies of the interstellar polarization surrounding other young LMC clusters and OB associations with similar hot star contents do not illustrate these types of complex field patterns (Wisniewski 2005; Wisniewski et al. 2007). Within the LMC 2 environment, the western side of NGC 2100 shows complex field patterns while the eastern side of the cluster only displays moderate evidence of cohesive field alignment. No asymmetry in the distribution of massive stars or their remnants in this cluster has been observed, thus we don't expect winds or outflows from NGC 2100's massive star population to be responsible for producing these field patterns. Rather, we speculate that other large-scale flows might play a major role in twisting field lines in the observed patterns.

Points et al. (1999) suggest that rather than being a cohesively expanding shell, the geometry of LMC 2 is that of two HI sheets enclosing a region of hotter gas. They suggest both cavity material and the surface of the HI sheets are being swept eastward across the complex by the outflows of material located on the western edge of the region. We speculate that such general, large-scale flows, carrying with them local magnetic field lines, might move past the northern and southern boundaries of NGC 2100 and be impeded by the cluster itself. Such a scenario could account for the coherent position angle patterns located to the north and south of NGC 2100, as well as the dramatic turnabout in the field immediately west of the cluster. As the neighborhood due east of NGC 2100 would be partially shielded from such flows, one would expect less coherent field patterns in this environment, as is observed to the east of NGC 2100. The 30 Dor complex, a rich site of powerful stellar outflows, is located to the west of NGC 2100. From polarization measurements, Mathewson & Ford (1970b) noted strong magnetic focusing in the 30 Dor region. Thus we suggest 30 Dor should be considered as a possible source of outflows which influence LMC 2 and shape the projected magnetic field patterns we observe.

A number of grain alignment mechanisms have been postulated and, as summarized in the review paper of Lazarian (2003), it is likely that different mechanisms may dominate in different astrophysical environments, depending upon the local conditions present. Some of the proposed mechanisms include the Davis-Greenstein process, in which paramagnetic dissipation by rotating grains leads to alignment (Davis & Greenstein 1951), the Gold process, in which grains are mechanically aligned via collisional interactions with a supersonic gas flow (Gold 1952; Lazarian 1994, 1997), and radiative torques, in which alignment is achieved via the spin-up of irregularly shaped grains which scatter left- and right-hand polarized light in a different way (Dolginov & Mytrophanov 1976; Draine & Weingartner 1996; Draine & weingartner 1997). The LMC-2 supershell itself, if it assumed to be a cohesively expanding body (e.g. Caulet et al. 1982), is only characterized by an expansion velocity of $\sim 30 \text{ km s}^{-1}$ (Caulet et al. 1982), which is well below the supersonic gas velocity required for the Gold mechanical alignment mechanism. However, NGC 2100's proximity to both the

30 Dor region and the winds of massive stars within NGC 2100 suggest that local grains might interact with a more dynamic gas flow than that which characterizes the much larger LMC-2 region. As such, we suggest that mechanical alignment might indeed play a partial role in constructing the observed morphology of aligned grains in the NGC 2100 region; clearly detailed modeling of the system would be advantageous to quantitatively constrain the various grain alignment mechanisms which could be operating in this dynamic environment.

4.2. Location of Polarizing Region

While we have interpreted the bulk of the magnetic field variability implied by our observations to be tied to the dynamics of the inner layer of LMC 2, we now consider the possible influence of the HI sheets which encompass this layer in the proposed 3-dimensional picture of Points et al. (1999). Based upon the derived total line of sight reddening for NGC 2100, $E_{B-V} = 0.24$ (Keller et al. 2000), the standard relationship between polarization and extinction presented in Serkowski et al. (1975), $P_{max} < 9 E_{B-V}$, predicts an interstellar polarization of $< 2.2\%$, in agreement with the average magnitude observed in our data set, $\sim 1.5\%$. Points et al. (1999) report the thin (80-100 pc) HI sheets have column densities of $\sim 1 \times 10^{21} \text{ cm}^{-2}$. This column density implies a reddening value similar to that of Keller et al. (2000), hence a similar predicted maximum magnitude of interstellar polarization, based upon the relation $N_{HI}/E_{B-V} = 5 \times 10^{21} \text{ atoms cm}^{-2} \text{ mag}^{-1}$ (Savage & Jenkins 1972). Thus it appears that enough dichroic absorption by interstellar dust grains could occur within the thin HI sheet positioned in front of NGC 2100 to produce the level of observed polarization.

4.3. Summary

We have presented polarization maps for a subsection of the LMC 2 supershell, namely NGC 2100 and its surround field. These maps show regions of aligned position angles on scales of $42 \times 24 \text{ pc}$ to $104 \times 83 \text{ pc}$, attributable to absorption by interstellar dust grains aligned by projected magnetic fields. We estimate these projected fields to have strengths of $8-17 \mu\text{G}$, and stress that more accurate field estimates may be achieved by incorporating measurements which better reflect the interstellar medium properties corresponding to our survey area. A plausible explanation for the observed complex field patterns is that outflows present within LMC 2, modified by velocity fields from NGC 2100, combine to produce the observed field patterns. The observed asymmetrical field morphology suggests the stellar sources in NGC 2100 are not the primary source of outflows shaping the observed fields. Rather, we speculate that NGC 2100 may serve to disrupt the path of large-scale flows moving eastward across LMC 2. We suggest that the 30 Dor region, observed to be a source of both massive outflows and strong magnetic fields, may be the source powering the observed field patterns in LMC 2.

Finally, we considered a proposed 3-dimensional picture of LMC 2 in which two HI shells confine a region of hotter gas. We find the magnitude of observed polarization could be produced by aligned dust grains within one of these HI shells, noting that some mechanism must then impart the complex field geometry produced within the

inner gas layer to this thin outer shell.

We thank the anonymous referee whose comments helped to improve this paper. This research was supported by NASA NPP and GSRP fellowships to JPW (NNH06CC03B, NGS5-50469), a NASA LTSA grant (NAG5-8054) and a Research Corporation Cottrell Scholar

award to KSB, and a FAPESP grant (02/12880-0) to AP. AMM also acknowledges support from the Brazilian agencies FAPESP and CNPq. Polarimetry at the University of São Paulo (USP) is supported by FAPESP. This research has made use of NASA's Skyview virtual observatory, NASA ADS, and the SIMBAD database.

REFERENCES

Aitken, D.K., Wright, C.M., Smith, C.H., & Roche, P.F. 1993, MNRAS, 262, 456
 Aitken, D.K., Smith, C.H., Moore, T.J.T., & Roche, P.F. 1995, MNRAS, 273, 359
 Ambroio-Cruz, P. et al. 2004, AJ, 127, 2145
 Cassatella, A., Barbero, J., Brocato, E., Catellani, V., & Geyer, E.H. 1996, A&A, 306, 125
 Caulet, A., Deharveng, L., Georgelin, Y. P., & Georgelin, Y.M. 1982, A&A, 110, 185
 Chandrasekhar, S. & Fermi, E. 1953, ApJ, 118, 113
 Crutcher, R.M. 2004, The Magnetized Interstellar Medium, ed. B. Uyaniker, W. Reich, & R. Wielebinski, 123
 Davis, L. & Greenstein, J.L. 1951, ApJ, 114, 206
 Dolginov, A.Z. & Mytrophanov, I.G. 1976, Ap&SS, 43, 291
 Draine, B.T. & Weingartner, J.C. 1996, ApJ, 470, 551
 Draine, B.T. & Weingartner, J.C. 1997, ApJ, 480, 633
 Feast, M.W. 1991, in IAU Sump. 148, The Magellanic Clouds, ed. R. Haynes, & D. Milne (Dordrecht: Kluwer), 1
 Gaensler, B.M., Haverkorn, M., Staveley-Smith, L., Dickey, J.M., McClure-Griffiths, N.M., Dickel, J.R., & Wolleben, M. 2005, Science, 307, 1610
 Gold, T. 1952, MNRAS, 112, 215
 Goodman, A.A. 1996, in ASP Conf. Ser. 97, Polarimetry of the Interstellar Medium, ed. W.G. Roberge & D.C.B. Whittet (San Francisco: ASP), 325
 Heitsch, F., Zweibel, E.G., Mac Low, M.-M., Li, P., & Norman, M.L. 2001, ApJ, 561, 800
 Henning, Th., Wolf, S., Launhardt, R., & Waters, R. 2001, ApJ, 561, 871
 Hildebrand, R.H., Dotson, J.L., Dowell, C.D., Schleuning, D.A., & Vaillancourt, J.E. 1999, ApJ, 516, 834
 Hodge, P.W. & Wright, F.W. 1967, Smithsonian Pub. 4699, The Large Magellanic Cloud (Washington: Smithsonian Press)
 Keller, S.C., Bessell, M.S., & Da Costa, G.S. 2000, AJ, 119, 1748
 Lazarian, A. 1994, MNRAS, 268, 713
 Lazarian, A., Goodman, A.A., & Myers, P.C. 1997, ApJ, 490, 273
 Lazarian, A. 1997, ApJ, 483, 296
 Lazarian, A. 2003, JQSRT, 79, 881
 Magalhães, A.M., Benedetti, E., & Roland, E. 1984, PASP, 96, 384
 Magalhães, A.M., Rodrigues, C.V., Margoniner, V.E., & Pereyra, A. 1996, in ASP Conf. Ser. 97, Polarimetry of the Interstellar Medium, ed. W.G. Roberge & D.C.B. Whittet (San Francisco: ASP), 118
 Mathewson, D.S. & Ford, V.L. 1970a, MmRAS, 74, 139
 Mathewson, D.S. & Ford, V.L. 1970b, ApJ, 160L, 43
 McLean, I.S. & Clarke, D. 1979, MNRAS, 186, 245
 Meaburn, J. 1980, MNRAS, 192, 365
 Meaburn, J., Marston, A.P., McGee, R.X., & Newton, L.M. 1987, MNRAS, 225, 591
 Melgarejo, R., Magalhães, A.M., Carciofi, A.C., & Rodrigues, C.V. 2001, A&A, 377, 581
 Mineshige, S., Shibata, K., & Shapiro, P.R. 1993, ApJ, 409, 663
 Pereyra, A. 2000, Ph.D. thesis, Univ. São Paulo
 Pereyra, A. & Magalhães, A.M. 2002, ApJS, 141, 469
 Pereyra, A. & Magalhães, A.M. 2007, ApJ, in press (astro-ph/0702550)
 Points, S.D. et al. 1999, ApJ, 518, 298
 Savage, B.D. & Jenkins, E.B. 1972, ApJ, 172, 491
 Serkowski, K., Mathewson, D.S., & Ford, V.L. 1975, ApJ, 196, 261
 Tamura, M., Hough, J.H., Greaves, J.S., Morino, J-I., Chrysostomou, A., Holland, W.S., & Momose, M. 1999, ApJ, 525, 832
 Tinbergen, J. 1982, A&A, 105, 35
 Tomisaka, K. 1998, MNRAS, 298, 797
 Vallee, J.P. 1993, ApJ, 419, 670
 Vallee, J.P. 1994, Ap&SS, 220, 289
 Wang, Q. & Helfand, D.J. 1991, ApJ, 379, 327
 Wisniewski, J.P., Bjorkman, K.S., & Magalhães, A.M. 2003, ApJL, 598, 43
 Wisniewski, J.P. 2005, Ph.D. thesis, University of Toledo
 Wisniewski, J.P., Bjorkman, K.S., Magalhães, A.M., Meade, M.R., & Pereyra, A. 2007, ApJ, submitted
 Yan, H. & Lazarian, A. 2006, ApJ, 653, 1292
 Zweibel, E.G. 1996, in ASP Conf. Ser. 97, Polarimetry of the Interstellar Medium, ed. W.G. Roberge & D.C.B. Whittet (San Francisco: ASP), 486

TABLE 1
JOURNAL OF NGC 2100 OBSERVATIONS

Filter	Obs. Date	Exposure Time
U	24 Nov. 2001	1200 sec.
B	23 Nov. 2001	240 sec.
V	23 Nov. 2001	180 sec.
R	24 Nov. 2001	180 sec.
I	23 Nov. 2001	180 sec.

Note. — Note that the listed exposure times correspond to the total integration at each of 8 wave-plate positions.

TABLE 2
SUMMARY OF MAGNETIC FIELD PROPERTIES BY REGION

Region	# Stars	Spatial Extent (pc)	Mean PA (deg)	FWHM (deg)	$\sigma(\tan\delta)$ (rad)	B (μ G)
A	105	73 x 177	0-90
B	110	104 x 83	76	24	0.24	25
C	88	63 x 75	122	37	0.26	23
D	56	104 x 63	94	22	0.20	30
E	56	42 x 24	167	46	0.44	14

Note. — Summary of the polarization position angle variability across our field of view.

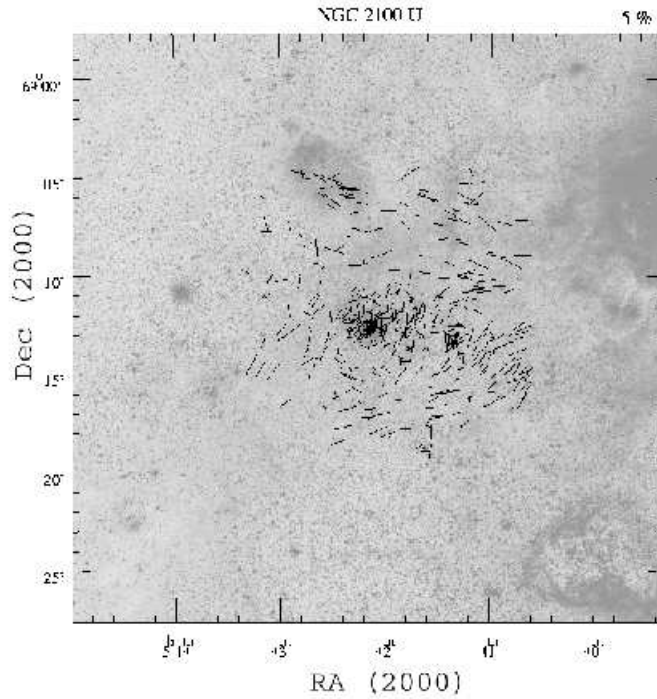


FIG. 1.— U filter polarization of 462 targets which have $p/\sigma_p > 3$ in the vicinity of NGC 2100. Polarization vectors are overplotted on a 0.5 deg² DSS2 blue image.

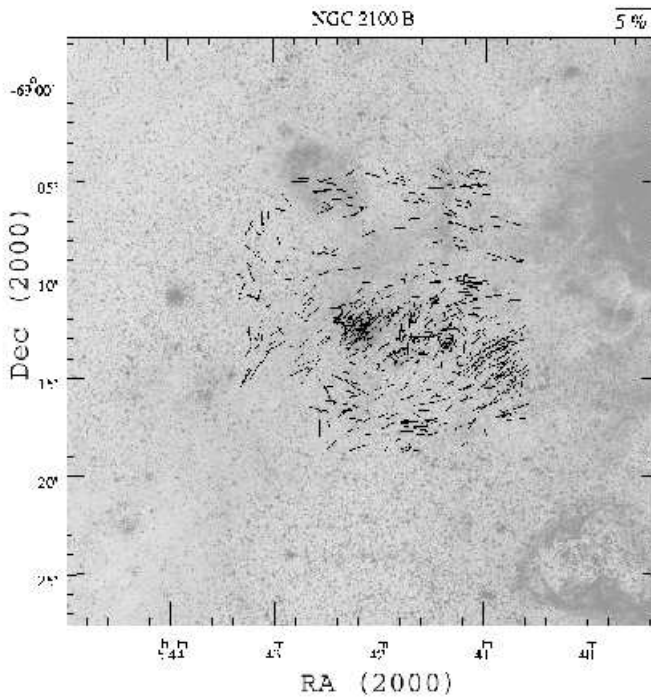


FIG. 2.— B filter polarization of 592 targets which have $p/\sigma_p > 3$ in the vicinity of NGC 2100. Polarization vectors are overplotted on a 0.5 deg² DSS2 blue image.

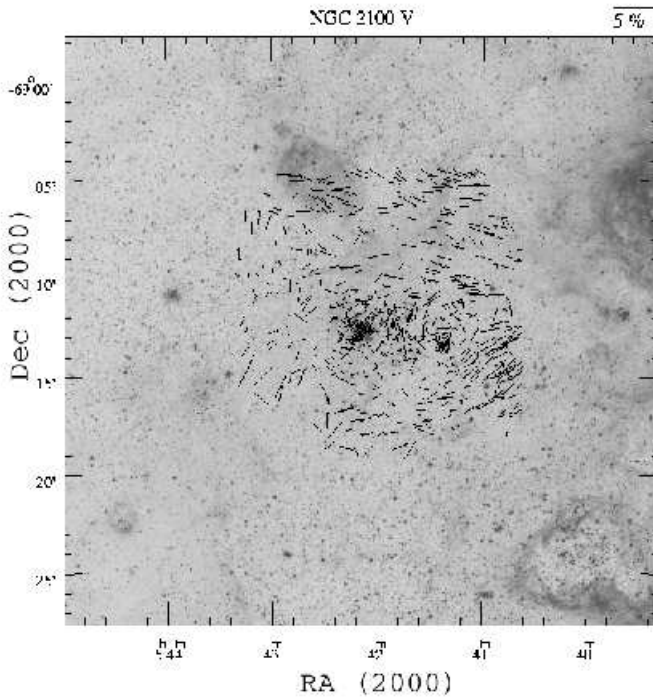


FIG. 3.— V filter polarization of 661 targets which have $p/\sigma_p > 3$ in the vicinity of NGC 2100. Polarization vectors are overplotted on a 0.5 deg² DSS2 red image.

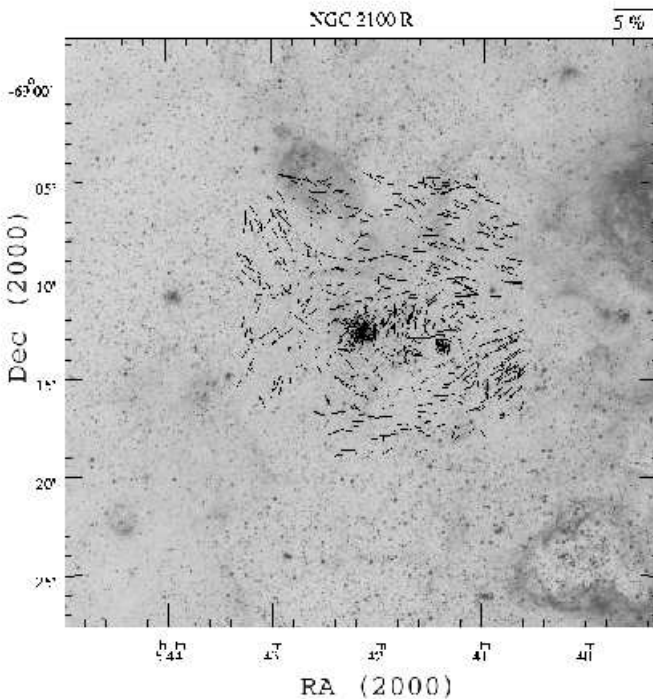


FIG. 4.— R filter polarization of 700 targets which have $p/\sigma_p > 3$ in the vicinity of NGC 2100. Polarization vectors are overplotted on a 0.5 deg² DSS2 red image.

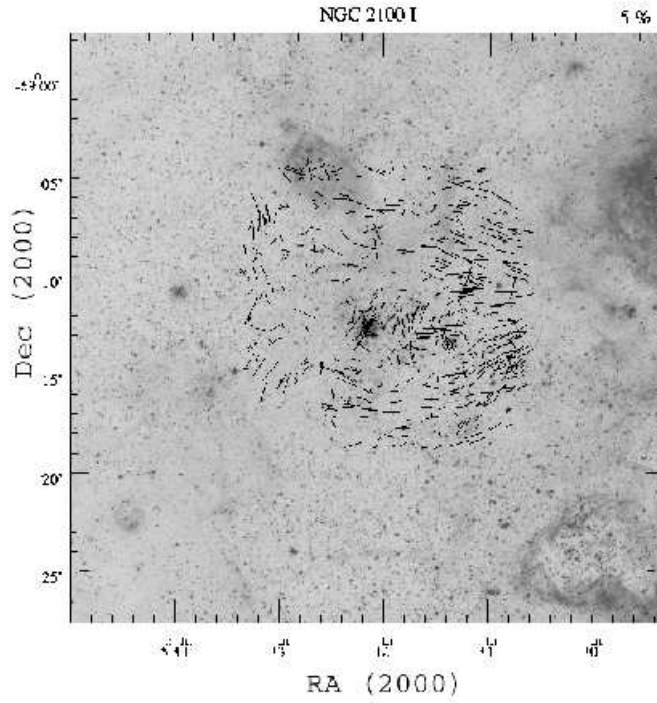


FIG. 5.— I filter polarization of 621 targets which have $p/\sigma_p > 3$ in the vicinity of NGC 2100. Polarization vectors are overplotted on a 0.5 deg² DSS2 red image.

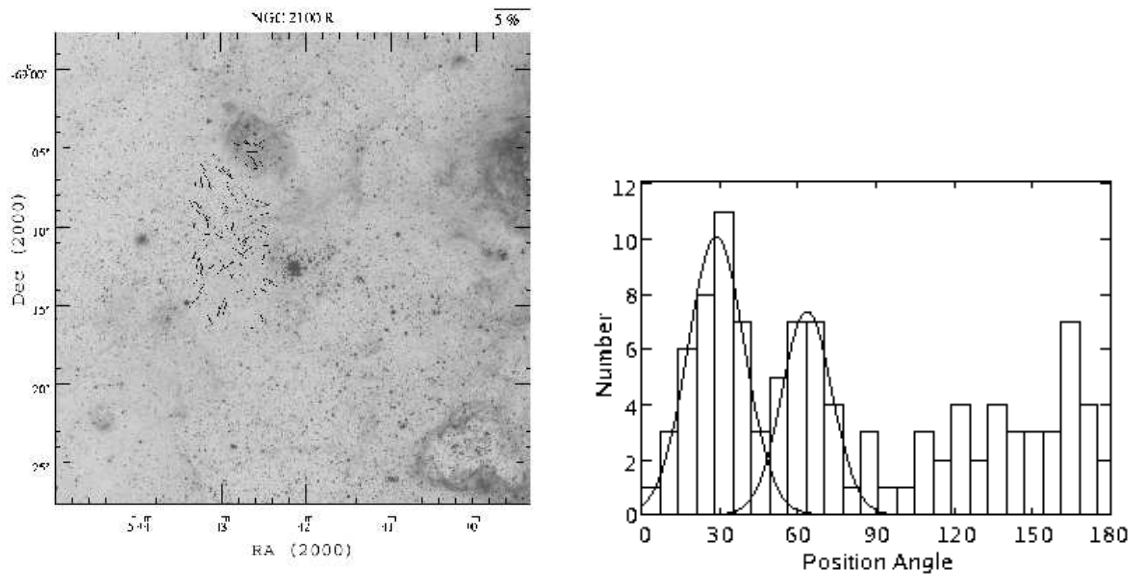


FIG. 6.— Section A of our field of view, showing the polarization of 105 objects with $0.1\% < p < 3.0\%$ and $p/\sigma_p > 3$. We find the position angles in this region are concentrated at angles $< 90^\circ$, possibly following a bimodal distribution with centers at 29° and 64° .

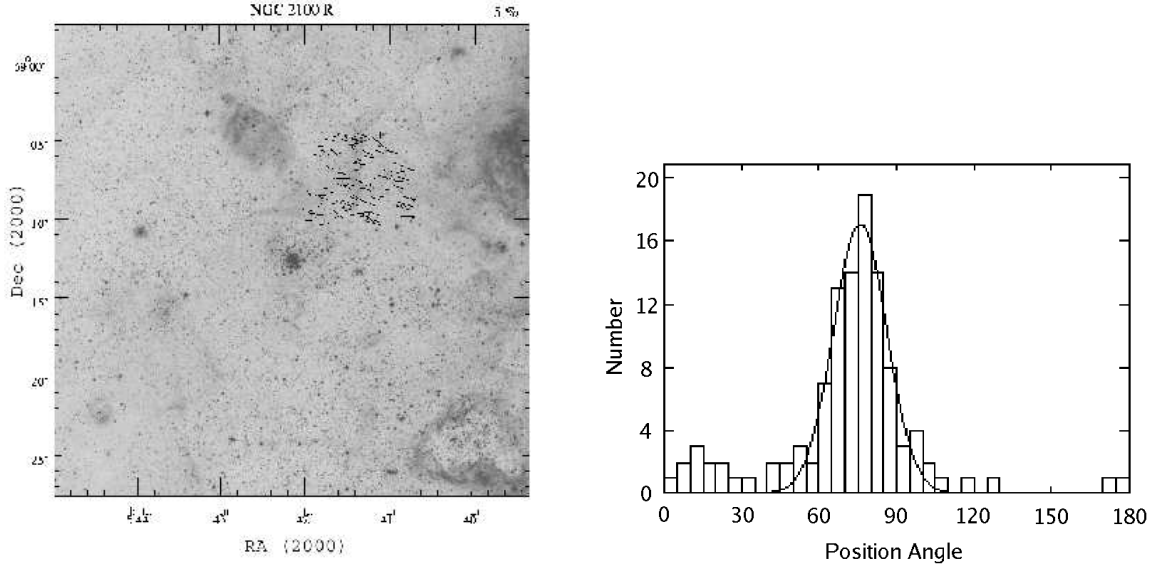


FIG. 7.— Section B of our field of view, showing the polarization of 110 objects with $0.1\% < p < 3.0\%$ and $p/\sigma_p > 3$. The mean polarization position angle of these stars, determined by a gaussian fit, is 76° .

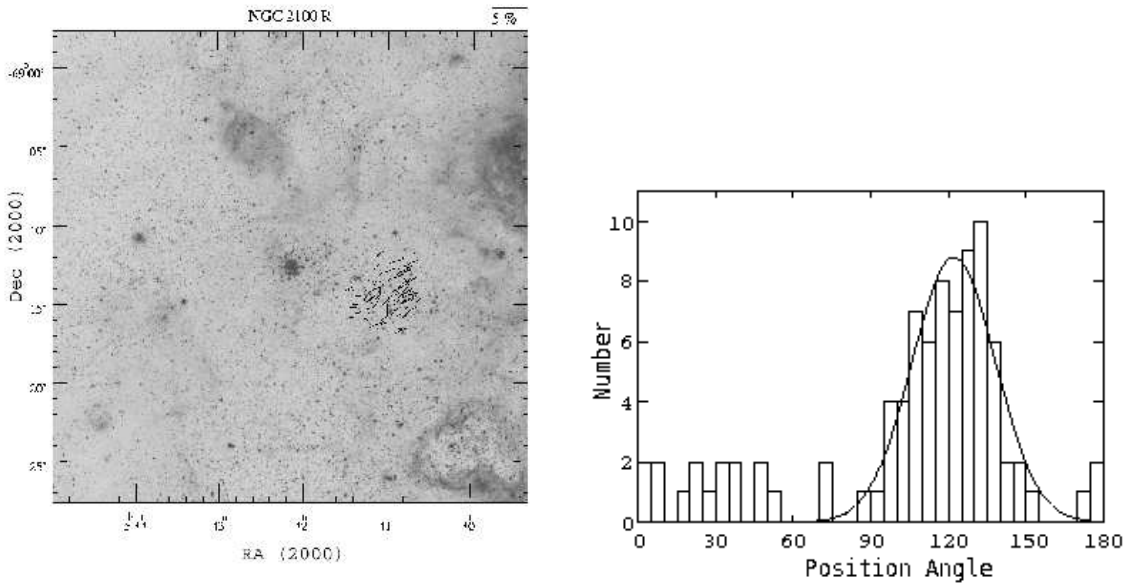


FIG. 8.— Section C of our field of view, showing the polarization of 88 objects with $0.1\% < p < 3.0\%$ and $p/\sigma_p > 3$. The mean polarization position angle of this region was determined to be 122° .

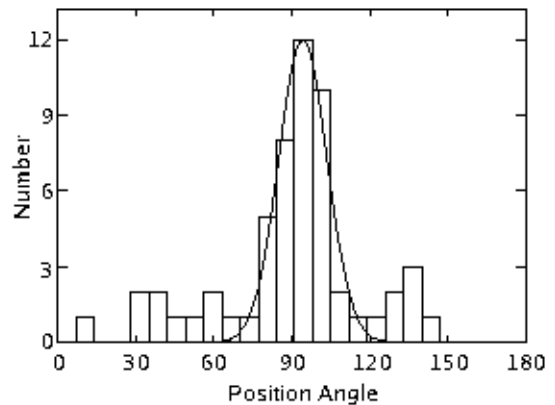
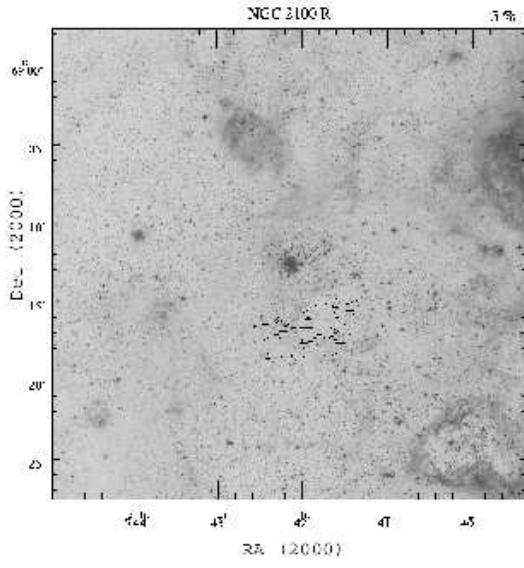


FIG. 9.—Section D of our field of view, showing the polarization of 56 objects with $0.1\% < p < 3.0\%$ and $p/\sigma_p > 3$. The mean polarization position angle of this region was determined to be 94° .

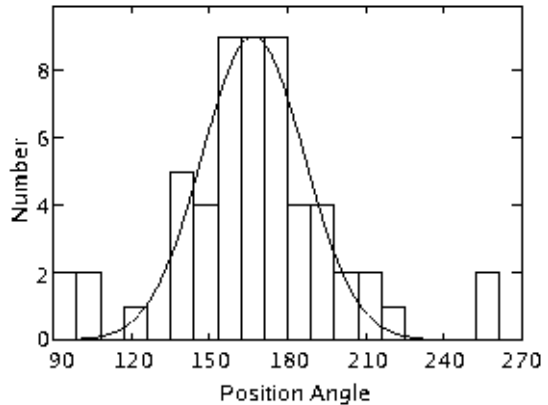
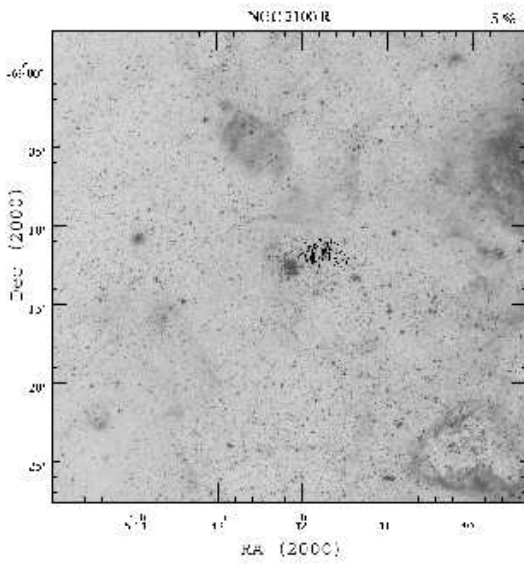


FIG. 10.—Section E of our field of view, showing the polarization of 56 objects with $0.1\% < p < 3.0\%$ and $p/\sigma_p > 3$. The mean polarization position angle of this region was determined to be 167° .